Millimeter-Wave-Radar Sensor Based on a Transceiver Array for Automotive Applications

Matthias Steinhauer, *Member, IEEE*, Hans-Oliver Ruoß, *Member, IEEE*, Hans Irion, and Wolfgang Menzel, *Fellow, IEEE*

Abstract—This paper describes a new radar sensor architecture comprising an array of transceiver modules. Target applications of the sensor are automotive driver assistance systems. In conjunction with a monolithic integration of each transceiver, the concept offers the possibility for a cost-effective realization of digital-beamforming radar sensors at millimeter-wave frequencies. A modulation sequence is investigated based on simultaneously transmitted frequency-modulated continuous-wave signals, which are separated by frequency multiplexing. Appropriate signal processing for the estimation of range, speed, and azimuth angle in multiple object situations is presented.

Experimental results with an eight-channel radar sensor in the 76–77-GHz frequency band are presented, which demonstrate the feasibility of the proposed architecture and show the performance of the modulation sequence and signal processing.

Index Terms—Array, automotive radar, digital beamforming (DBF), frequency-modulated continuous wave (FMCW), transceiver.

I. INTRODUCTION

MILLIMETER-WAVE (MMW) radar is an important sensing principle for automotive driver assistance systems. The main automotive application of radar sensors today is adaptive cruise control, which is based on forward-looking long-range sensors in the 76–77-GHz frequency band covering a range up to 150 m and an azimuth field of view of $\pm 8°$. According to the evolution of driver assistance systems towards active safety systems, the radar sensors will also be employed for functions such as collision warning, brake assistance, or automatic emergency braking. These applications demand a higher detection performance compared to current radar sensors. The azimuthal angular resolution has to especially be improved significantly to values below $2°$ to achieve a better object separation [1], [2]. Simultaneously, a larger field of view is required.

A suitable sensor architecture for improved angular detection performance is an antenna array with beamforming or high-resolution direction of arrival (DOA) estimation in the digital do-
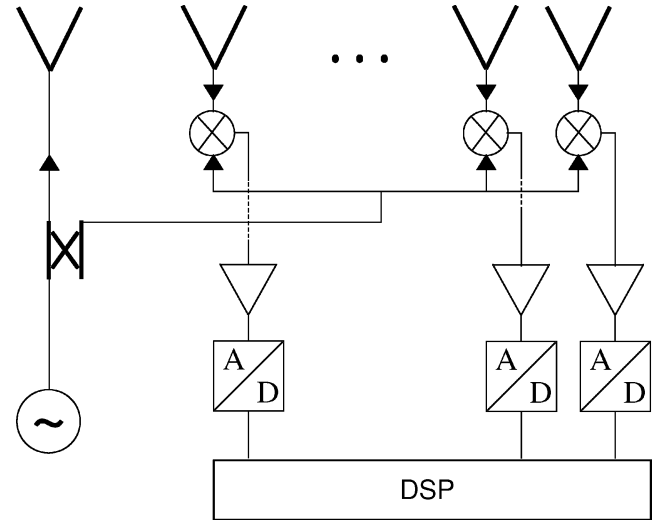
Fig. 1. Block diagram of a typical DBF radar sensor frontend.

main. A typical digital beamforming (DBF) frontend architecture is shown in Fig. 1. The main circuit blocks are a signal source, which feeds a single transmit antenna, and an array of receivers where a part of the transmit signal is used as a local oscillator signal to down-convert the RF signals to baseband.

The cost associated with this architecture has prohibited its implementation for automotive radar sensors thus far. Different concepts based on switching in the transmit or receive paths have been proposed to reduce the required number of receiver channels [2]–[7]. However, switching operation at MMW frequencies of 76 GHz introduces significant losses, which are disadvantageous in the receive path due to an increased noise figure and in the transmit path due to the limited transmit power of monolithic signal sources. Switching typically also requires an increased bandwidth in the baseband, which additionally increases noise power and, therefore, reduces system sensitivity.

A different approach to reduce the cost of an array sensor architecture is pursued with the sensor concept proposed in this paper. The proposed architecture comprises an array of transmit–receive modules, which can be cost-effectively implemented by monolithically integrating each transceiver module including antenna structures, thereby avoiding interconnects at MMW frequencies.

II. SENSOR CONCEPT

A block diagram of the radar sensor frontend is depicted in Fig. 2. The channels of the array are realized as identical transmit–receive modules instead of receivers in a conventional
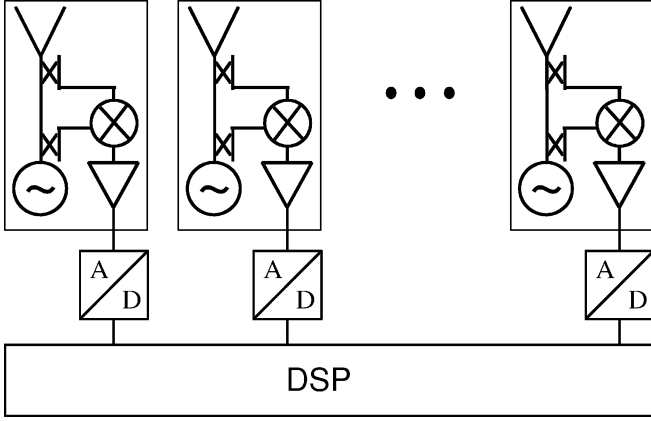
Fig. 2. Principle block diagram of proposed transceiver array frontend.

Fig. 3. Time section of the transmit signals with frequency multiplex between the different transceiver modules.

array frontend architecture. This arrangement is advantageous from a cost perspective in combination with a monolithic integration of each transceiver including antenna structures. The monolithic integration of the transceiver modules allows an assembly without the need of interconnects and wire bonds in the carrier frequency range of 76 GHz as no MMW signal has to be distributed between the transceivers. Therefore, the assembly is simplified, and a standard printed circuit board substrate material can be used. The multiple deployment of one monolithic microwave integrated circuit (MMIC) also leads to a high modularity of the sensor concept.

In principle, all basic radar modulation signals as FMCW, pulse Doppler, or pseudonoise phase coding can be used as transmit signals of the transceiver modules. The FMCW modulation is chosen here because of the low complexity required for the transceiver modules and the efficient use of available signal power. The availability of independent signal sources for each array module facilitates the formation of different transmit–receive configurations of the array. A favorable configuration is the monostatic transmit–receive mode of each transceiver with homodyne conversion of the received signals, as depicted in Fig. 2. The main advantage of this configuration is the elimination of the carrier signal phases by the homodyne mixing process whereby the need for exact phase synchronization of the sources is avoided. A prerequisite of this mode is the decoupling of the modules to avoid transmitter interference.

The modulation schemes developed for switched FMCW arrays represent a time-domain multiplex of the channels and could, therefore, be applied to the transceiver array. Examples are the processing of sequential fast frequency-modulated continuous-wave (FMCW) sweeps [6], [7] or the fragmentation of a single FMCW sweep upon the different channels [2].

Here, a different modulation scheme is proposed, making use of the available signal sources in each channel. The time–frequency relation of the transmit signals of the different sources is depicted in Fig. 3. All sources are transmitting simultaneously, and transmitter interference is avoided by frequency multiplexing of the carrier frequencies. Advantages of this modulation scheme are the avoidance of switching operations and the minimized cycle time due to the simultaneous transmission. By the prevention of switching, a better system sensitivity can
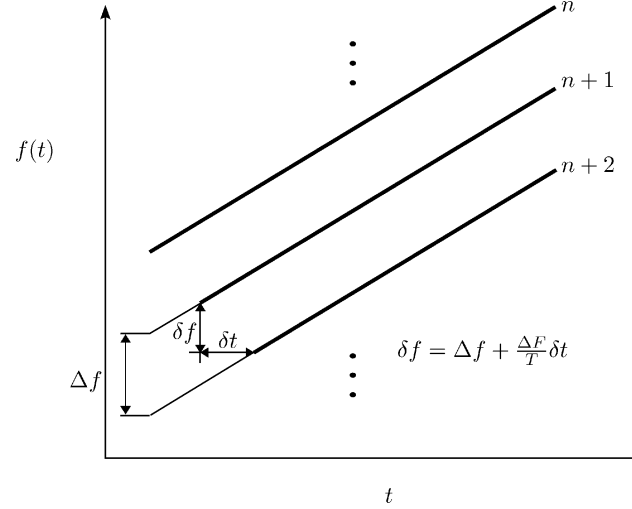
be achieved, and no additional signal processing effort is required to eliminate potential ambiguities resulting from aliasing effects.

The FMCW transmit signal of the nth source can be described as

$$s_{t,n}(t) = A_n \cdot e^{j2\pi \frac{\Delta F}{2T} t^2} \cdot e^{j[2\pi(f_0 + n \cdot \Delta f) \cdot t + \varphi_{0,n}]} \tag{1}$$

where ΔF and T are the bandwidth and duration of the modulation, respectively, f_0 is the reference carrier frequency, Δf is the frequency shift between the carrier frequencies of adjacent modules, and $\varphi_{0,n}$ is the constant carrier signal phase of the nth source. A received echo signal of the nth module, resulting from a reflection of its own transmit signal at a moving object, is an attenuated and time-delayed replica of the transmit signal with a Doppler shift of the carrier frequency

$$s_{r,n}(t) = \alpha \cdot A_n \cdot e^{j2\pi \frac{\Delta F}{2T} \left(t - \frac{2R}{c_0}\right)^2}$$
$$\cdot e^{j\left[2\pi(f_0 + n \cdot \Delta f)\left(1 - \frac{2v}{c_0}\right) \cdot \left(t - \frac{2R}{c_0}\right) + \varphi_{0,n}\right]} \tag{2}$$

where α is the attenuation, R is the object range to the reference module, v is the object speed, and c_0 is the free-space propagation velocity.

The baseband signal results from the multiplication of transmit and receive signal. For further analysis, only the phase of the resulting signal is relevant. Taking the module at the left edge of the array as the reference, the phase of the baseband signal of the nth module can be expressed after some approximations as

$$\Phi_{B,n} = -2\pi \cdot \left[\left(\frac{\Delta F}{T} \frac{2R}{c_0} + \frac{2vf_0}{c_0} \right) \cdot t \right.$$
$$\left. + \frac{2Rf_0}{c_0} + \frac{2n}{\lambda_0} \left(d \sin\theta + R \frac{\Delta f}{f_0} \right) \right] \tag{3}$$

where θ is the azimuth angle of the incoming signal, λ_0 is the free-space wavelength, and d is the element spacing of the array.

Baseband signals resulting from transmit signals of all other modules can be suppressed by a low-pass filter as they are shifted by the transmit frequency difference Δf.

The time-dependent phase term in (3) represents the baseband frequency, which is dependent on distance and velocity of an object

$$f_\mathrm{B} = \frac{\Delta F}{T} \frac{2R}{c_0} + \frac{2vf_0}{c_0}. \tag{4}$$

The progression of the time-independent baseband signal phase along the array corresponds to the phases of the steering vector components and is dependent on the angle of arrival θ of the incoming signal. Additionally the phase progression is dependent on the distance R of the reflecting object. This relation is caused by the carrier frequency shift between the transceiver modules. By evaluating time-shifted sections of the baseband signals, an effective time and frequency shift is realized between the FMCW signals of adjacent modules, as depicted in Fig. 3. For the effective time and frequency shift and the physical frequency shift, the following relation holds:

$$\delta f = \Delta f + \frac{\Delta F}{T} \delta t \tag{5}$$

where δf and δt are the effective frequency and time shifts, respectively. This leads to a total phase progression along the array, which is dependent on azimuth angle, distance, and velocity of an object

$$\Phi_{\mathrm{B},n} - \Phi_{\mathrm{B},n-1} = 2 \cdot \frac{2\pi}{\lambda_0} \left[d\sin\theta + R\frac{\delta f}{f_0} + v\delta t \right]. \tag{6}$$

The result is a virtual shift of the detected azimuth angle according to

$$\sin\theta_m = \sin\theta + \frac{1}{d} \left[v\delta t + R\frac{\delta f}{f_0} \right] \tag{7}$$

with the estimated azimuth angle θ_m, the real azimuth angle θ, and the object velocity and distance v and R.

Furthermore, the phase lags between adjacent modules are doubled compared to a conventional receiver array with a single transmit source. This results from the simultaneous variation of transmitter and receiver location due to the monostatic processing of the respective transmit and receive signals as the phase lags of transmit and receive path are added [3]–[5]. The addition of the phase lags is, in the current case, equivalent to a doubling of the physical aperture of the array. Therefore, a required angular resolution can be achieved with a smaller physical aperture. As the number of elements is kept constant, the unambiguous angular range determined by the distance of grating lobes of the array factor is reduced to

$$|\theta| < \arcsin\left[\lambda_0/(4d)\right]. \tag{8}$$

III. Modulation Sequence and Signal Processing

The additional dependence of the estimated azimuth angle from object distance and speed according to (7) can be deployed for the unambiguous estimation of distance and speed. A drawback of the FMCW modulation is the coupling of R and v in the
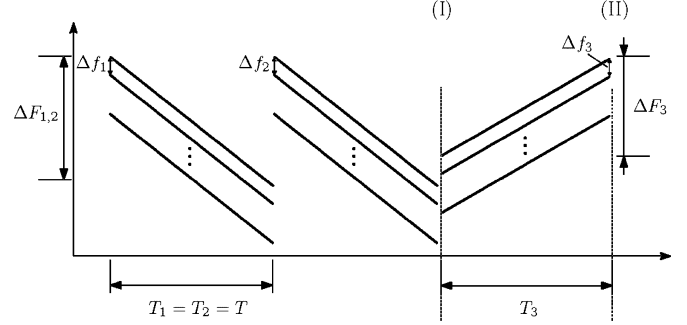

Fig. 4. Modulation sequence.

baseband frequency according to (4). A common approach to resolve the ambiguity of the baseband frequency is the processing of several FMCW sweeps with different modulation parameters, e.g., a triangular waveform with an ascending and a descending frequency sweep [8]. This yields two linear equations, which can be solved unambiguously only for a single object. In multiple object situations with M objects, this leads to $M^2 - M$ possible objects, and the so-called ghost targets have to be resolved by further FMCW sweeps. This results in a high processing effort, and the risk of unresolved ghost targets remains.

The unambiguous estimation of distance and speed is possible by the utilization of frequency- or time-shifted FMCW sweeps by using the additional phase information [9], [10]. The underlying principle is the dependency of the baseband phase difference from distance and velocity when applying a time or frequency shift. With the system concept and modulation scheme proposed here, the virtual shift of the estimated azimuth angle from the actual value can be deployed to extract the relevant phase information.

A suitable modulation sequence is represented by the first two FMCW sweeps depicted in Fig. 4. In the first step of the signal processing, baseband frequencies and associated azimuth angles are estimated for any reflected signal within each sweep. Due to the identical sweep rate of each channel, equal baseband frequencies result for each channel. The baseband frequencies can be efficiently estimated by a fast Fourier transform (FFT) and subsequent peak detection. The associated azimuth angles are estimated by the application of DBF algorithms to the amplitude and phase information in the frequency domain.

For the ease of calculation, the wavenumber in direction of the array

$$k_x = \frac{2\pi}{\lambda_0} \sin\theta \tag{9}$$

is used instead of the azimuth angle, assuming the x-axis is oriented along the array. Rewriting (7) results in

$$k_{x,m} = k_x + \frac{2\pi}{\lambda_0 d} \left[v\delta t + R\frac{\delta f}{f_0} \right]. \tag{10}$$

Together with the baseband frequency, one FMCW sweep results in two linear independent equations, which are connected for each object, containing R and v. The equations cannot be directly solved, as after (10), the estimated wavenumber $k_{x,m}$ is also dependent on the unknown actual wavenumber k_x. Two

consecutive FMCW sweeps according to the first two sweeps in Fig. 4 can be used to eliminate k_x, as its value can be assumed to stay constant during the measurement cycle. Using a different carrier frequency shift between adjacent transceivers in each sweep, two linear independent equations result, which can be subtracted to yield

$$d(k_{x,1} - k_{x,2}) = \frac{2\pi}{\lambda_0} \left[v(\delta t_1 - \delta t_2) + \frac{R}{f_0}(\delta f_1 - \delta f_2) \right]. \quad (11)$$

From (11) and (4), R and v can be directly estimated as

$$\hat{R} = \frac{Tc_0}{2\pi} \cdot \frac{d(k_{x,1} - k_{x,2}) + \pi f_B(\delta t_1 - \delta t_2)}{\Delta F(\delta t_2 - \delta t_1) + T(\delta f_1 - \delta f_2)} \quad (12)$$

$$\hat{v} = \frac{c_0}{2\pi f_0} \cdot \frac{d\Delta F(k_{x,2} - k_{x,1}) + \pi f_B T(\delta f_2 - \delta f_1)}{\Delta F(\delta t_2 - \delta t_1) + T(\delta f_1 - \delta f_2)}. \quad (13)$$

The actual azimuth angle can subsequently be calculated from (7) using the estimated distance and velocity.

In general, the achievable accuracy of distance and velocity estimation using (12) and (13) is lower compared to the use of two independent baseband frequencies. This is due to the lower accuracy of angle or phase estimation compared to frequency estimation. Therefore, if a higher accuracy is required, a third FMCW sweep can be used, as depicted in Fig. 4. Using the resulting baseband frequency, the estimation accuracy from the first step according to (12) and (13) is improved.

A. Unambiguous Range

The phase difference or angle difference, respectively, involved in the distance and velocity estimation according to (12) and (13) is ambiguous. The unambiguous phase range corresponds to $-\pi < \Delta\varphi < \pi$, where $\Delta\varphi$ is the phase difference between the baseband signals of adjacent transceivers. The relevant phase difference between the baseband signals of two adjacent transceivers can be derived from (11) as

$$\Delta\varphi = \frac{4\pi}{\lambda_0} \left[v(\delta t_2 - \delta t_1) + \frac{R}{f_0}(\delta f_2 - \delta f_1) \right]. \quad (14)$$

Considering the unambiguous phase range, the effective time and frequency shifts for unambiguous distance and velocity estimation must satisfy the following relation:

$$\left| R_{\max} \cdot \frac{\delta f_2 - \delta f_1}{f_0} + v_{\max} \cdot (\delta t_2 - \delta t_1) \right| \leq \frac{\lambda_0}{4} \quad (15)$$

where the unambiguous distance range is assumed as $0 < R < R_{\max}$ and the unambiguous velocity range as $|v| < v_{\max}$.

B. Estimation Accuracy

The variance of the estimation of R and v using (12) and (13) can be derived by error propagation as

$$\sigma_R^2 = \left(\frac{Tc_0}{2\pi(\Delta F \cdot \delta t - T \cdot \delta f)} \right)^2 (2d^2\sigma_{k_x}^2 + \pi^2\delta t^2\sigma_f^2) \quad (16)$$

$$\sigma_v^2 = \left(\frac{\lambda_0}{2\pi(\Delta F \cdot \delta t - T \cdot \delta f)} \right)^2 (2d^2\Delta F^2\sigma_{k_x}^2 + \pi^2T^2\delta t^2\sigma_f^2). \quad (17)$$

TABLE I
ARRAY, MODULATION, AND SIGNAL PARAMETERS
DEPLOYED FOR VARIANCE CALCULATION

Symbol	Value	Quantity
c_0	$3 \cdot 10^8$ m/s	velocity of propagation
f_0	$76.5 \cdot 10^9$ Hz	carrier frequency
λ_0	3.9 mm	carrier wavelength
d	3.9 mm	array element spacing
ΔF	200 MHz	FMCW modulation bandwidth
T	1.3 ms	modulation length
M	512	samples of baseband-signal
N	8	number of transceiver modules
SNR	10 dB	signal to noise ratio
$R_{\max}$	200 m	unambiguous distance range
$v_{\max}$	250 km/h	unambiguous velocity range

The estimation accuracy is dependent on the variance of frequency estimation σ_f and angle estimation σ_{kx}, respectively. For the modulation parameters and unambiguous distance and velocity ranges listed in Table I, the minimum standard deviation is achieved for maximum admissible effective time shift and zero effective frequency shift between adjacent transceiver signals. Here, the maximum admissible effective time shift equals $\delta t = 14.04$ μs after (15).

Using an FFT of length 512 with subsequent maximum detection and center of gravity estimation, a standard deviation for the frequency estimation of approximately $\sigma_f = 0.01/T$ can be achieved for a signal of length T. As a practical estimation accuracy for estimation of the azimuth angle, a standard deviation of $\sigma_\theta = 0.05°$ corresponding to a standard deviation of $\sigma_{kx} = 1.41$ m^{-1} is assumed here, which is achieved with the experimental radar sensor described in Section IV. The resulting standard deviations for the estimation of R and v can, therefore, be calculated as

$$\sigma_R = 17 \cdot 10^{-2} \text{ m} \quad (18)$$
$$\sigma_v = 34 \cdot 10^{-2} \text{ m/s}. \quad (19)$$

It has to be considered that deviations of the nominal frequency offset between the carrier frequencies lead to a bias in the estimation of distance and velocity. A synchronization of the carrier frequencies is, therefore, required to achieve the estimation accuracy derived above.

IV. EXPERIMENTAL RADAR SENSOR

A prototypical radar sensor for the 76–77-GHz frequency range has been realized to investigate the feasibility of the system concept with emphasis on the modulation sequence and signal-processing scheme. A block diagram of the sensor is depicted in Fig. 5. The sensor comprises eight parallel transmit–receive circuits, which are realized in a hybrid assembly of MMICs and discrete components on an organic
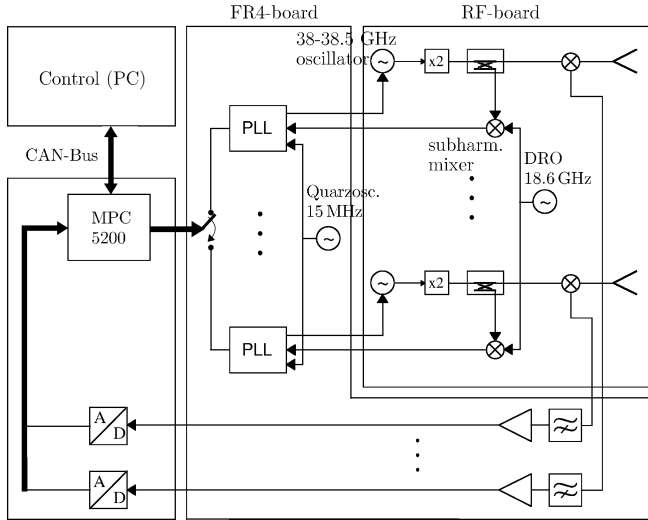
Fig. 5. Block diagram of experimental radar sensor consisting of eight separate transmit–receive modules.

Fig. 6. RF circuit board.

high-frequency substrate. A hybrid assembly on a high-frequency laminate is used, as no fully monolithic transceiver modules were available yet. The essential properties of the sensor concept can be evaluated independent from the assembly technology. In parallel, a development of monolithic transceiver modules for MMW frequencies is ongoing. In a first step, the feasibility of key components as oscillators and mixers for frequencies beyond 100 GHz is shown in an SiGe–BiCMOS technology [11].

At the current prototypic sensor, MMIC oscillators at a nominal frequency of 38 GHz are used as signal sources. For each channel, a subsequent frequency doubler and power amplifier MMIC transfers the oscillator signal to the target frequency range and provides a typical output power of 18 dBm. The mixers are realized as transfer mixers consisting of a single series diode. A part of the source signal is coupled with a directional coupler and a bandpass filter to a harmonic mixer, where it is converted to an intermediate frequency of 2 GHz. A 18.6-GHz dielectric resonator oscillator provides the local oscillator signal for all eight channels. Its signal is distributed to the eight subharmonic mixers by a three-stage Wilkinson power-divider network. The nonlinear component of the subharmonic mixers is a single diode of the same type, as it is used for the receiving mixers. A 15-MHz quartz oscillator is used as a common reference source for the phase locked-loop (PLL) circuits.

The antennas consist of half-wavelength microstrip patches as radiating elements with dielectric rods on top. The dielectric rods have a lower cylindric and an upper conical section with an overall length of approximately 8 mm. The geometric parameters as length, diameter, and taper of the conical section have been optimized with the help of a full-wave electromagnetic simulation to achieve an efficient illumination of the subsequent lens. A cylindric dielectric lens is deployed to obtain a narrow elevation beam and an increased antenna gain. The influence on the azimuth radiation characteristic is intentionally low to achieve the largest possible beam overlap of the eight channels. A spacing of the patch antennas of one free-space wavelength is chosen.
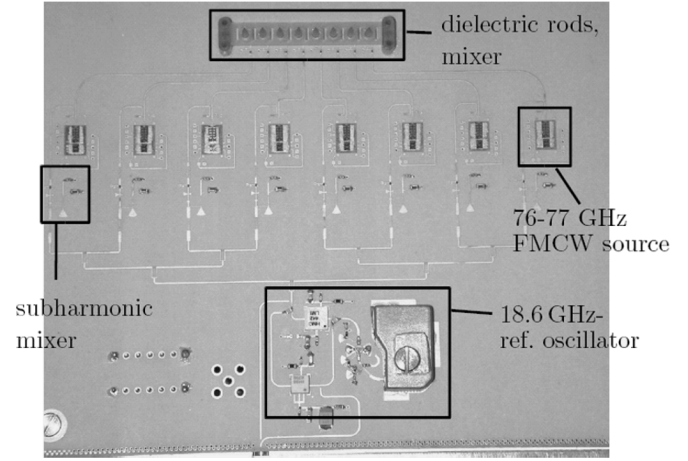
A photograph of the RF frontend is depicted in Fig. 6. In the center, the MMICs for the signal sources are recognizable. The output signals are transferred to the antenna circuits by microstrip lines whose length varies between the transceivers due to assembly constraints. The polyrod antennas are visible at the top of the picture.

The attenuation of the transmission lines between signal source and transfer mixers varies from 1.5 to 5 dB due to the different line lengths. The insertion loss of the transmit path of the mixer amounts to 3 dB. With the typical output power of the frequency doubler of 18 dBm from 76 to 77 GHz, the signal power at the antenna feed points can be estimated to vary from 10 to 13.5 dBm among the channels.

The low-frequency circuits as PLL application-specific integrated circuits (ASICs), baseband amplifiers and filters are assembled on an FR4 substrate, which is laminated to the backside of the RF substrate. For the sensor control and data acquisition, a separate board with a Motorola MPC5200 microprocessor is used. The microprocessor is controlled from a PC using LabView, and a controller area network (CAN) interface is used for communication.

The bandwidth of the system is limited by the maximum sweep bandwidth of the PLL-ASIC to approximately 500 MHz.

V. MEASUREMENT RESULTS

A. Phase Noise of Transmit Signals

For characterization of the phase noise of the sources, the transmitted signals at a fixed frequency of approximately 76.5 GHz are received by means of a horn antenna close to the sensor. A 40-GHz spectrum analyzer with an external W-band downconverter is used to measure the power spectrum.

The power spectrum of one channel is depicted in Fig. 7. The phase noise can be estimated to approximately -80 dBc/Hz at 100-kHz offset from the carrier. At this measurement, the frequency spacing between the transmit signals of different channels is 18 MHz. With decreasing frequency spacing, the phase noise increases due to parasitic coupling between the PLLs. For
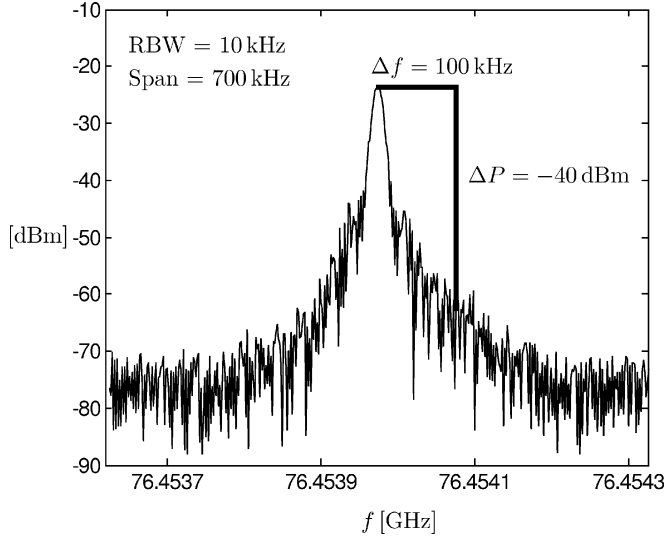
Fig. 7. Power spectrum of transmit signal of one transceiver channel.

Fig. 9. Normalized array pattern for reflector at $0°$ with 25-dB Chebyshev weighting applied to the baseband signals.
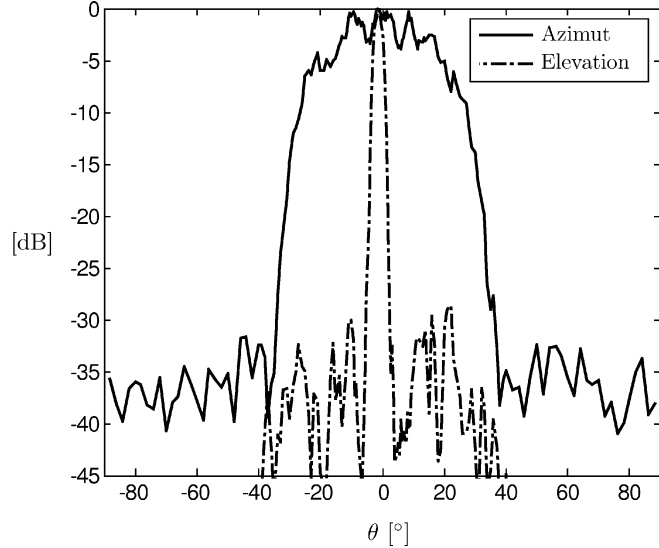

Fig. 8. Normalized two-way single-channel azimuth and elevation radiation pattern.

all measurement results, presented below, the same frequency spacing of 18 MHz is chosen.

B. Antenna Radiation Pattern

1) Single-Channel Pattern: With monostatic operation of the transceiver modules, the effective antenna characteristics correspond to the two-way radiation pattern. This characteristic is measured here for all eight transceivers by analyzing the peak power of the FMCW baseband signals resulting from the reflected power of a corner reflector in a fixed distance of 6 m. The measured two-way azimuth and elevation characteristics of one channel are depicted in Fig. 8. The antenna characteristic is normalized to the maximum baseband signal power. A simulation of the antenna system including losses shows an absolute antenna gain of 20 dB.
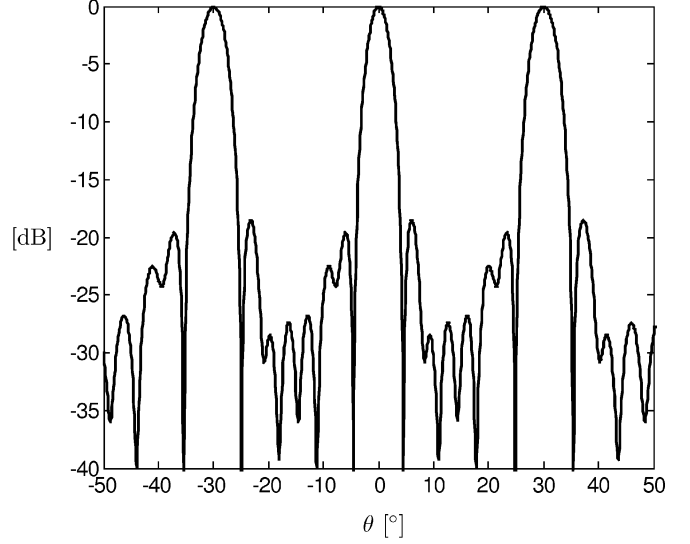
The azimuth pattern has a sector-like form with a 6-dB two-way beamwidth, corresponding to the one-way 3-dB beamwidth of approximately $52°$, and a steep transition from the main lobe to the sidelobe region. The elevation pattern has a 6-dB two-way beamwidth of $4°$ due to the dielectric lens. The highest sidelobes are approximately 30 dB below the main lobe for the two-way pattern.

2) Array Pattern: The array pattern resulting after array calibration is depicted in Fig. 9. A Chebyshev window with 25-dB sidelobe suppression is applied to the signals of the eight channels. Array calibration has been performed using the algorithm described in [12]. The 3-dB beamwidth of the main lobe is $3.9°$ and the first zero of the array pattern is located at $4.6°$. Grating lobes occur at $±30°$ and $±90°$, which result from the effective spacing of the antennas of two wavelengths due to the synthetic doubling of the physical spacing when monostatic transmit–receive processing is applied. The Chebyshev weighting is effective only for sidelobes beyond $±10°$. The close-in sidelobes are limited to approximately 20 dB below the main lobe due to calibration imperfections. It has to be noted that the dynamic range with respect to interfering signals beyond $±30°$ is substantially enhanced due to the single-channel pattern.

C. Range and Velocity Estimation

1) Static Objects: The estimation of range and velocity using the principle modulation scheme, as presented in Section III, has been investigated experimentally for static and dynamic objects. The static measurement setup consists of a corner reflector in a distance of approximately 6 m to the sensor. The size of the reflector is varied to analyze the influence of signal-to-noise ratio. The whole setup is placed in an anechoic chamber. Sweep bandwidth and duration of the FMCW sweep are chosen as $\Delta F = 200$ MHz and $T = 1.3$ ms for all eight signal sources. The carrier frequency difference between the transmit signals of adjacent modules is chosen large enough to allow a decoupling of the transceiver signals by filtering in the baseband.
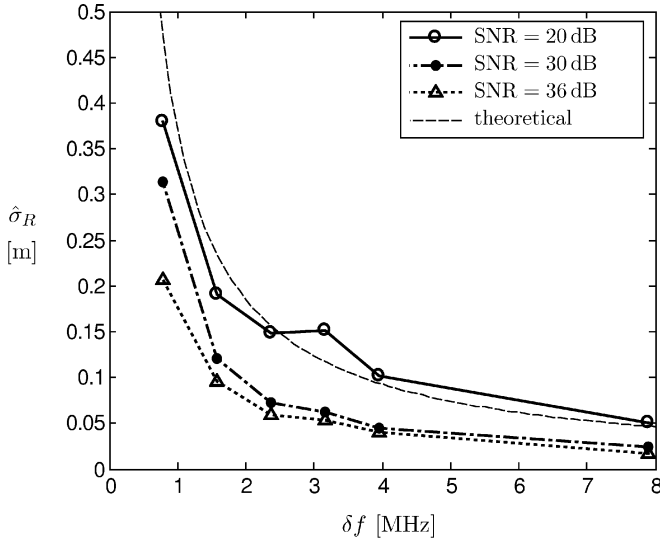
Fig. 10. Standard deviation of the direct estimation of R from (12) in dependence of effective frequency shift δf and signal-to-noise ratio.
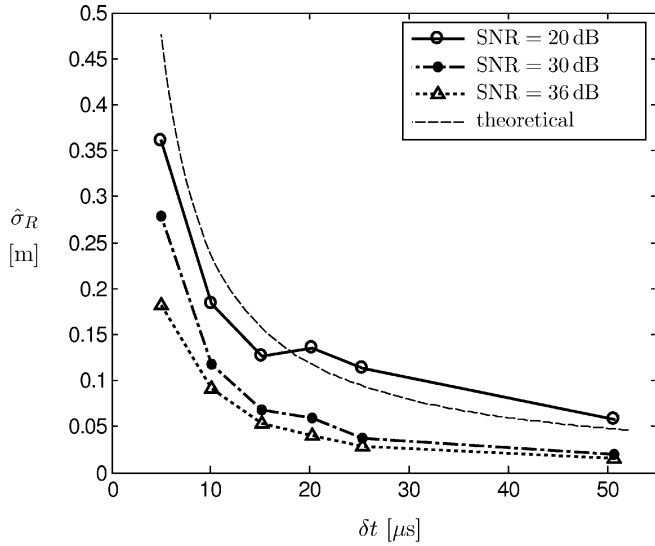

Fig. 11. Standard deviation of the direct estimation of R from (12) in dependence of effective time shift δt and signal-to-noise ratio.

The standard deviation for the distance estimation is depicted in Figs. 10 and 11 for different effective frequency shifts and different effective time shifts, respectively. The measured standard deviation for velocity estimation is not depicted. It shows qualitatively equal results due to the coupling of R and v according to (4). The standard deviation is estimated from the results of 15 measurements for each parameter. Here, time and frequency shift denote the difference of the effective time or frequency shift of adjacent transmit signals between the first two commensurable frequency sweeps according to Fig. 4. Physically, the frequency shift is varied. The effective time and frequency shifts are applied by analyzing appropriately time-shifted sections of the baseband signals. Additionally, the theoretical curves for the standard deviation after (16) at a signal-to-noise ratio of 20 dB are depicted, assuming a standard deviation of angle estimation of $\sigma_\theta = 0.05°$ and of baseband frequency estimation of
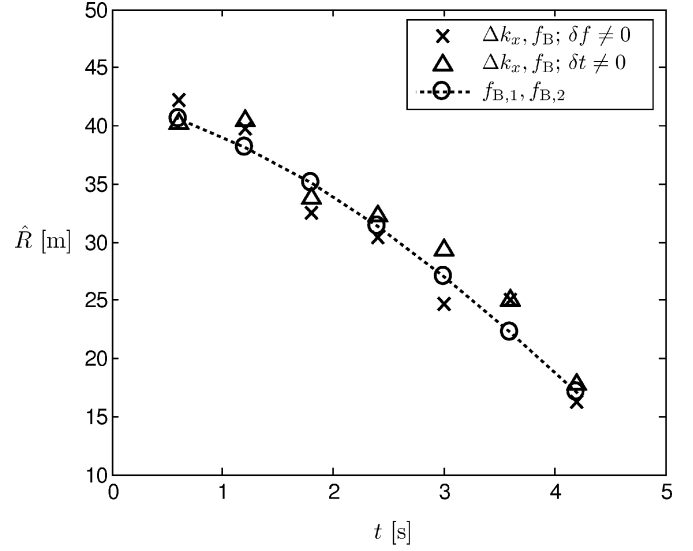

Fig. 12. Estimated distance of an approaching target for estimation of R from (12) and using two independent baseband frequencies.

$\sigma_f = 0.008/T$, which are realistic values for the experimental sensor.

The measured curves show the principal reciprocal relationship of the standard deviation to the effective time and frequency shifts according to (16). The standard deviation decreases, as expected, with increasing signal-to-noise ratio. Considering the required unambiguous distance range of 200 m and unambiguous velocity range of 250 km/h, the maximum permissible time shift is $\delta t = 14$ μs and the maximum frequency shift is $\delta f = 375$ kHz. For a signal-to-noise ratio of 20 dB, the resulting standard deviation for a time shift of 14 μs is $\sigma_R = 15$ cm. The corresponding standard deviation for the velocity estimation yields $\sigma_v = 0.3$ m/s.

2) Dynamic Objects: The estimation of R and v using the proposed signal-processing scheme utilizes differential phase information from two consecutive FMCW sweeps, as depicted in the modulation cycle in Fig. 4. A prerequisite for unbiased range and velocity estimation is that the azimuth angle of a target shows a negligible change between the two measurements as the azimuth angle is assumed as equal. To confirm the validity of this assumption, measurements with dynamic objects have been conducted. In Fig. 12, the results of distance estimation over time for a measurement setup with a static sensor and a car approaching the sensor are depicted. During the measurement, the car is accelerating from 10 to 30 km/h. The results of direct estimation of R and v are shown for an effective frequency shift of only $\delta f = 790$ kHz and for an effective time shift of only $\delta t = 5$ μs. Additionally the results of the following distance and velocity estimation are depicted using the baseband frequencies of the second FMCW sweep and a third sweep with different frequency slope. The results show that the distance and velocity estimation deploying differential phase information is reliably applicable to dynamic scenarios.

D. Azimuth Angle Estimation

For the evaluation of angular resolution in the azimuth direction, a measurement setup with two equidistant corner reflec-
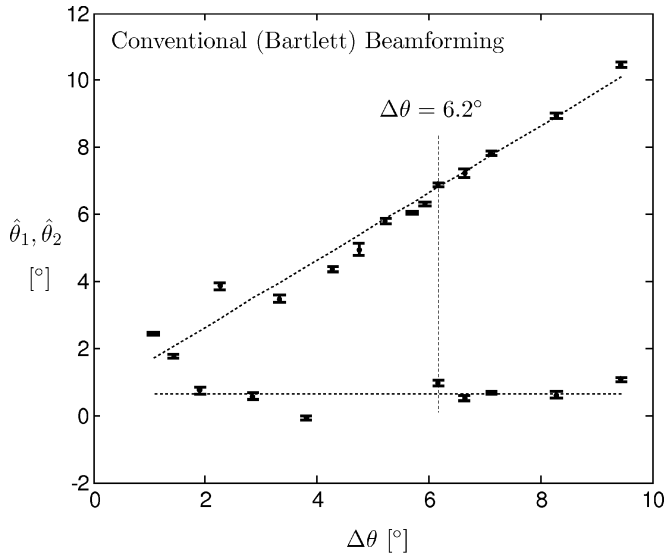
Fig. 13. Estimated azimuth angles of two equidistant corner reflectors with an increasing lateral displacement. Conventional beamforming with 25-dB Chebyshev weighting.

Fig. 14. Estimated azimuth angles of two equidistant corner reflectors with an increasing lateral displacement. Root-MUSIC algorithm.

tors in a distance of 5 m to the sensor is used. The lateral displacement of the reflectors is varied from 8 cm to 80 cm, corresponding to azimuth angle differences between approximately $1°$ and $9.4°$.

The processing of the azimuth angle is applied to the baseband signals after transformation to the frequency domain. In principle, all beamforming and DOA estimation techniques can be applied to the signals. Here, at first the performance of the Bartlett beamforming algorithm, below referred to as conventional beamforming, is investigated.

Previous study has shown the potential of high-resolution DOA techniques like MUSIC and ESPRIT [13] applied to automotive radar sensors for carrier frequencies of 24 GHz [14] and 77 GHz [2]. By the possible improvement of the resolution limit beyond that of conventional beamforming, the required aperture size can be reduced. To show the angular resolution achievable with the current prototypic sensor, the baseband signals have, therefore, additionally been processed using the Root-MUSIC algorithm [15].

In Fig. 13, the results of the azimuth angle estimation using the conventional beamforming algorithm with 25-dB Chebyshev weighting of the eight channels are depicted. The variation of the estimation results of 15 measurements is shown by the length of the bars. The two corner reflectors are resolved for angular displacements larger than approximately $6.2°$. For an array with a physical aperture of $7\lambda_0$, a theoretical resolution limit of approximately $9.8°$ for the single aperture and of $4.9°$ for the double aperture can be estimated from the occurrence of the first zero of the array pattern. It is evident that the resolution limit of the single aperture is nearly improved by a factor of 2.

The results of the DOA estimation using the Root-MUSIC algorithm are depicted in Fig. 14. The covariance matrix of the array has been averaged over two sub-arrays of seven elements to increase the robustness of the estimation against nonwhite noise and coherent signals. The results show an angular resolution limit of $1.7°$, which is more than a threefold improvement over conventional beamforming.

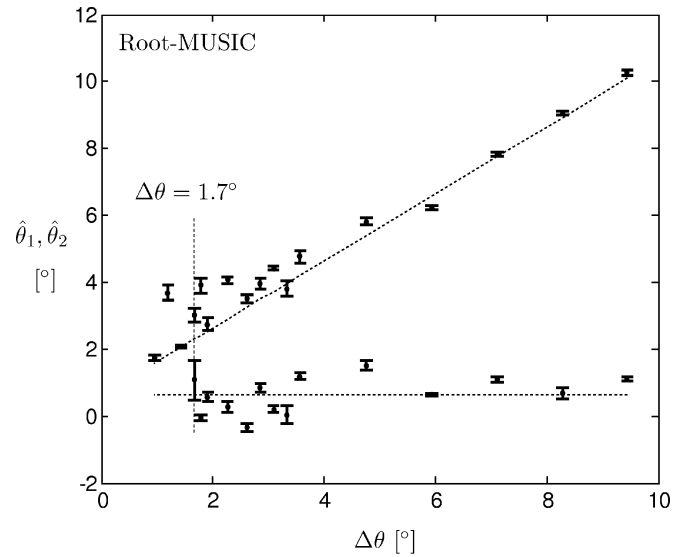## VI. CONCLUSION

A radar sensor concept based on an array of transceiver modules has been presented, which enables the cost-effective realization of electronic beamforming radar sensors at MMW frequencies in conjunction with a monolithic integration of each transceiver. A suitable modulation sequence, based on FMCW signals and appropriate signal processing has been described, which enables the unambiguous estimation of range and velocity in multiple object situations.

An experimental radar sensor comprising eight transceiver channels in a hybrid assembly for the 76–77-GHz frequency band has been realized to show the feasibility of the sensor concept. The performance of the modulation sequence has been evaluated and the achieved estimation accuracy is in good agreement with the theoretical results. The performance of azimuth angle estimation and the high object separation capability has been shown for the Bartlett beamformer and for the Root-MUSIC DOA estimation algorithm.

REFERENCES

[1] J. Wenger, "Automotive radar—Status and perspectives," in *IEEE CSIC Symp. Dig.*, 2005, pp. 21–24.
[2] Y. Asano, S. Oshima, T. Harada, and M. Ogawa, "Proposal for holographic radar with antenna switching," *Res. Develop. Rev. Toyota CRDL*, vol. 37, no. 2, pp. 1–6, 2002.
[3] N. Kees, E. Schmidhammer, and J. Detlefsen, "Improvement of angular resolution of a millimeter wave imaging system by transmitter location multiplexing," in *IEEE MTT-S Int. Microw. Symp. Dig.*, 1995, pp. 969–972.
[4] W. Mayer, A. Gronau, W. Menzel, and H. Leier, "A compact 24 GHz sensor for beam-forming and imaging," in *9th Int. Control, Autom., Robot., Vision Conf.*, Singapore, Dec. 2006, pp. 153–158.
[5] S. Tokoro, K. Kuroda, A. Kawakubo, K. Fujita, and H. Fujinami, "Electronically scanned millimeter-wave radar for pre-crash safety and adaptive cruise control system," in *IEEE Intell. Veh. Symp.*, 2003, pp. 304–309.
[6] L. Yang, L. Liwan, P. Weifeng, C. Yaqin, and F. Zhenghe, "Signal processing method for switch antenna array of the FMCW radar," in *Proc. IEEE Radar Conf.*, 2001, pp. 289–293.

[7] V. Katkovnik, M. S. Lee, and Y. H. Kim, "High-resolution signal processing for a switch antenna array FMCW radar with a single channel receiver," in *Proc. Sensor Array and Multichannel Signal Process. Workshop*, 2002, pp. 543–547.

[8] M. Skolnik, *Radar Handbook*. New York: McGraw-Hill, 1970.

[9] S. Kemkemian and P. Lacomme, "Method and device for frequency modulated continuous-wave radar detection with removal of ambiguity between distance and speed," U.S. Patent 005963163A, Oct. 10, 1999.

[10] H. Rohling and M.-M. Meinecke, "Waveform design principles for automotive radar systems," in *CIE Int. Radar Conf.*, 2001, pp. 1–4.

[11] M. Steinhauer, H. Irion, M. Schott, M. Thiel, O. Ruoss, and W. Heinrich, "SiGe-based circuits for sensor applications beyond 100 GHz," in *IEEE MTT-S Int. Microw. Symp. Dig.*, 2004, pp. 223–226.

[12] C. M. S. See, "Method for array calibration in high-resolution sensor array processing," in *IEEE Proc. Radar, Sonar, Navigation*, 1995, vol. 142, no. 3, pp. 90–96.

[13] H. Krim and M. Viberg, "Two decades of array signal processing research," *IEEE Signal Process. Mag.*, pp. 67–94, 1996.

[14] M. Schneider *et al.*, "Automotive short range radar (SRR) sensors at 24 GHz with smart antennas," in *Proc. German Radar Symp.*, Bonn, Germany, 2002, pp. 175–179.

[15] A. J. Barabell, "Improving the resolution performance of eigenstructure-based direction-finding algorithms," in *Proc. ICASSP'83*, Boston, MA, 1983, pp. 336–339.

Matthias Steinhauer (S'03–M'06) received the M.S. (Dipl.-Ing.) degree in electrical engineering from the Technical University of Aachen, Aachen, Germany, in 2002, and the Ph.D. (Dr.-Ing.) degree from the University of Ulm, Ulm, Germany, in 2007.

From 2002 to 2005, he was with the RF Group, Research and Development Division, Robert Bosch GmbH. Since 2005, he has been a Development Engineer of magnetic rotational speed sensors with Chassis Systems Control, Robert Bosch GmbH, Abstatt, Germany. His research interests include radar sensor system aspects, FMCW-radar signal processing, and monolithic MMW oscillator design.

Hans-Oliver Ruoß (M'96) was born in Esslingen, Germany, on April 3, 1968. He received the M.S. (Dipl.-Ing.) and Ph.D. (Dr.-Ing.) degrees in electrical engineering from the University of Stuttgart, Stuttgart, Germany, in 1994 and 1998, respectively.

From 1994 to 1998, he was with the Institut für Hochfrequenztechnik, where his main interests were antennas, electromagnetic compatibility (EMC), and numerical techniques in electromagnetics. Since 1998, he has been with the Robert Bosch Company, Reutlingen, Germany, where from 2001 to 2006, he was Head of the RF Group, Research and Development Division. His research interests during this time were RF and radar sensors, RF power applications, and wireless data transmission. From 2006 to 2007, he was Head of the EMC Group for electronic control unit (ECU) development within Gasoline Systems, Robert Bosch Company, where, since 2007, he has been Director of the Electromagnetic Compatibility Division, Automotive Electronics.

Dr. Ruoß was the recipient of the 1995 Best Paper Award presented at the ITG Conference on Mobile Communications, Ulm, Germany, and the 1997 Antenna Conference Prize presented at the Institution of Electrical Engineers (IEE) 10th International Conference on Antennas and Propagation, Edinburgh, U.K.

Hans Irion was born in Stuttgart, Germany, on September 11, 1967. He received the M.S. degree [Dipl.-Ing. (FH)] in communications engineering from the University of Applied Sciences Esslingen, Esslingen, Germany, in 1995.

Since 1995, he has been with the Robert Bosch Company, Schwieberdingen, Germany, where from 1995 to 2004, he was a member of the RF Group, Research and Development Division. His research interests there were RF and radar sensors and integrated RF circuits. Since 2005, he has been a Project Manager for electromagnetic compatibility simulation with Gasoline Systems, Robert Bosch Company.

Wolfgang Menzel (M'89–SM'90–F'01) received the Dipl.-Ing. degree in electrical engineering from the Technical University of Aachen, Aachen, Germany, in 1974, and the Dr.-Ing. degree from the University of Duisburg, Duisburg, Germany, in 1977.

From 1979 to 1989, he was with the Millimeter-Wave Department, AEG [now the European Aerospace, Defense, and Space Systems (EADS)], Ulm, Germany . From 1980 to 1985, he was Head of the Laboratory for Integrated Millimeter-Wave Circuits. From 1985 to 1989, he was Head of the entire Millimeter-Wave Department. During that time, his areas of interest included planar integrated circuits (mainly on the basis of fin-line techniques), planar antennas, and systems in the MMW frequency range. In 1989, he became a Full Professor with the Institute of Microwave Techniques, University of Ulm, Ulm, Germany. His current areas of interest are multilayer planar circuits, waveguide filters and components, antennas, MMW and microwave interconnects and packaging, and MMW application and system aspects.

Dr. Menzel was an associate editor for the IEEE TRANSACTIONS ON MICROWAVE THEORY AND TECHNIQUES (2003–2005). From 1997 to 1999, he was a Distinguished Microwave Lecturer for Microwave/Millimeter Wave Packaging. From 1997 to 2001, he chaired the German IEEE Microwave Theory and Techniques (MTT)/Antennas and Propagation (AP) Chapter. He was the recipient of the 2002 European Microwave Prize.